A New View of the Size–Mass Distribution of Galaxies: Using r_{20} and r_{80} Instead of r_{50}

Tim B. Miller[1], Pieter van Dokkum[1] ⓘ, Lamiya Mowla[1] ⓘ, and Arjen van der Wel[2,3] ⓘ

[1] Department of Astronomy, Yale University, 52 Hillhouse Avenue, New Haven, CT 06511, USA; tim.miller@yale.edu
[2] Sterrenkundig Observatorium, Universiteit Gent, Krijgslaan 281 S9, B-9000 Gent, Belgium
[3] Max-Planck-Institut für Astronomie, Königstuhl 17, D-69117, Heidelberg, Germany

Abstract

When investigating the sizes of galaxies it is standard practice to use the half-light radius, r_{50}. Here we explore the effects of the size definition on the distribution of galaxies in the size–stellar mass plane. Specifically, we consider r_{20} and r_{80}, the radii that contain 20% and 80% of a galaxy's total luminosity, as determined from a Sérsic profile fit, for galaxies in the 3D-*HST*/CANDELS and COSMOS-DASH surveys. These radii are calculated from size catalogs based on a simple calculation assuming a Sérsic profile. We find that the size–mass distributions for r_{20} and r_{80} are markedly different from each other and also from the canonical r_{50} distribution. The most striking difference is in the relative sizes of star-forming and quiescent galaxies at fixed stellar mass. Whereas quiescent galaxies are smaller than star-forming galaxies in r_{50}, this difference nearly vanishes for r_{80}. By contrast, the distance between the two populations *increases* for r_{20}. Considering all galaxies in a given stellar mass and redshift bin we detect a significant bimodality in the distribution of r_{20}, with one peak corresponding to star-forming galaxies and the other to quiescent galaxies. We suggest that different measures of the size are tracing different physical processes within galaxies; r_{20} is closely related to processes controlling the star formation rate of galaxies and r_{80} may be sensitive to accretion processes and the relation of galaxies with their halos.

Key words: galaxies: fundamental parameters – galaxies: high-redshift – galaxies: structure

1. Introduction

The sizes of galaxies hold clues about the physical processes that shape them. They can be predicted by galaxy formation models (Mo et al. 1998; Dutton et al. 2011; Kravtsov 2013; Somerville et al. 2018) and can help distinguish between different evolutionary models (Carollo et al. 2013; van Dokkum et al. 2015; Matharu et al. 2018). However, the sizes of galaxies are difficult to define, as their surface brightness profiles decrease smoothly with radius and have no well-defined edge. A common method is to use the half-light, also known as the effective radius, r_{50}, which contains 50% of a galaxy's total luminosity. It is generally applicable to all galaxies and does not trivially correlate with other properties such as a galaxy's luminosity. Due to these properties, r_{50} has become the standard measurement of the size of a galaxy. Studies of r_{50} over the past decades have shown that it correlates with stellar mass, the so-called size–mass distribution, which in turn varies with galaxy color, type, and redshift (Shen et al. 2003; Ferguson et al. 2003; Trujillo et al. 2006; Williams et al. 2010; Ono et al. 2013; van der Wel et al. 2014; Lange et al. 2015; Mowla et al. 2018).

When investigating the size–mass distribution it is important to assess the effect of the choice of the size parameter, as a single number fails to capture information about the distribution of light within a galaxy. In practice, a second parameter is typically introduced to separately study the form of the light profile. The Sérsic index n (Sérsic 1968) has become the parameter of choice, derived from 1D or 2D fits of the form $\log I(r) \propto (r/r_{50})^{1/n}$ to the surface brightness profile.

In this Letter we explore an alternative approach to studying the structure of galaxies. We compare and contrast the size–mass distribution that arises from using different measures for the size of a galaxy. We will use r_{20} and r_{80}, the radii that contain 20% and 80% of the total luminosity, along with the canonical measure of r_{50}. This Letter will focus on the

difference between star-forming and quiescent galaxies at a fixed stellar mass to investigate the different evolutionary processes that shape them. In an accompanying Letter, Mowla et al. (2019), we investigate the relation between r_{80} and a galaxy's dark matter halo.

2. Data

2.1. Galaxy Sample

In this Letter we employ two different galaxy surveys: 3D-*HST*/CANDELS (Koekemoer et al. 2011; Brammer et al. 2012) and COSMOS-DASH (Momcheva et al. 2016; Mowla et al. 2018). The CANDELS survey covers 0.22 degree^2 with extensive ground- and space-based photometry ranging from 0.3 to 8 μm, which is supplemented by WFC3 grism spectroscopy spanning three-quarters of that area. Galaxy sizes are measured in van der Wel et al. (2014) from the H_{160} and I_{814} bands for $\sim$30,000 galaxies above $M_* > 10^9 M_\odot$ with $0 < z < 3$. Galaxy properties such as stellar mass, redshift, and rest-frame colors for this sample are taken from the 3D-*HST* catalog (Skelton et al. 2014). We supplement this sample with the COSMOS-DASH survey, which covers 0.66 deg^2 with H_{160} imaging. The larger survey area affords proper sampling of the bright end of the luminosity function for $1.5 < z < 3$, which is not possible in the smaller CANDELS survey. Combined with 1.7 deg^2 of ACS-COSMOS imaging (Koekemoer et al. 2007), Mowla et al. (2018) measured the sizes of 910 galaxies with $M_* > 2 \times 10^{11} M_\odot$ at $0 < z < 3$. Masses and redshifts for the COSMOS-DASH sample are taken from the UltraVISTA catalog (Muzzin et al. 2013a), as described in Mowla et al. (2018).

van der Wel et al. (2014) and Mowla et al. (2018) used very similar methods to measure the size of galaxies. GALFIT (Peng et al. 2010) is used to fit 2D single-component Sérsic profiles to each galaxy and extract a best-fit Sérsic index and
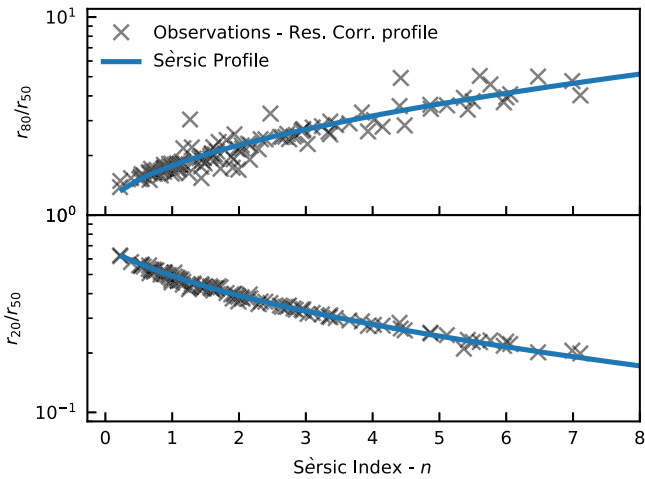
Figure 1. Ratios $r_{20\%}/r_{\rm eff}$ and $r_{80\%}/r_{\rm eff}$ are shown as a function of Sérsic index. The blue lines display the calculation for a Sérsic function based on Equation (2). Gray crosses display measurements of isolated galaxies in the GOODS-South field using direct integration of the residual-corrected surface brightness profile. We find that the observations match the calculation based on the Sérsic index very well.

effective radius. This forward modeling approach allows the measurement of galaxy sizes that are comparable to the instrumental point-spread function (PSF). The ACS/F814W filter is used for galaxies with $z < 1.5$, and the WFC3/F160W filter is used at higher redshift. Redshift- and mass-dependent color gradients are taken into account to ensure that the sizes of all galaxies are measured at the same rest-frame wavelength (5000 Å). Throughout this Letter we will separate galaxies into two populations: star-forming and quiescent. This is done using their rest-frame *UVJ* colors according to the prescription in Muzzin et al. (2013b).

2.2. Calculating r_{20} and r_{80}

Given that the sizes of galaxies at high redshift are comparable to the PSF, one cannot simply measure r_{20} and r_{80} directly from the surface brightness profile. Thus we choose to calculate r_{20} and r_{80} from the Sérsic profile derived by GALFIT (Peng et al. 2010). For a single-component Sérsic profile it is straightforward to convert between r_{50}, r_{20} and r_{80}. The fraction of light contained within a projected radius r is

$$\frac{L(<r)}{L_{\rm tot}} = \frac{\gamma(2n, b_n(r/r_{\rm eff})^{1/n})}{\Gamma(2n)}. \tag{1}$$

Here, γ is the incomplete gamma function, Γ is the complete gamma function, and b_n is the solution to the equation $\Gamma(2n) = 2\gamma(2n, b_n)$, which we approximate as $b_n = 1.9992n - 0.3271$ (Capaccioli 1989). Comparing $L(<r_{20})$ to $L(<r_{50})$ we derive the following.

$$\frac{L(<r_{20})}{L(<r_{50})} = \frac{0.2}{0.5} = \frac{\gamma(2n, b_n(r_{20}/r_{50})^{1/n})}{\gamma(2n, b_n)}. \tag{2}$$

For a given value of n, we numerically solve Equation (2) for the value of r_{20}/r_{50}. A similar procedure is used to calculate r_{80}/r_{50}. We perform this calculation for a range of Sérsic indices, with results shown in Figure 1. For higher Sérsic

indices r_{20}/r_{50} decreases, corresponding to the steeper central profile, and r_{80}/r_{50} increases, corresponding to the extended wings at large radius. We present fitting formulas for r_{20}/r_{50} and r_{80}/r_{50} as a function of Sérsic index, shown below in Equation (3). These fitting functions are accurate to within 5% for $n = 0.25$–10:

$$\frac{r_{20}}{r_{50}}(n) = -0.0008n^3 + 0.0178n^2 - 0.1471n + 0.6294$$

$$\frac{r_{80}}{r_{50}}(n) = 0.0012n^3 - 0.0123n^2 + 0.5092n + 1.2646. \tag{3}$$

Galaxies, especially those at high redshift, do not necessarily follow a Sérsic profile, thus it is important to check whether applying the simple calculation discussed above is broadly applicable. We tested this by employing the technique used in Szomoru et al. (2010) to correct surface brightness profiles for the effects of the PSF. Galaxies are fit with a single-component Sérsic profile, which is then convolved with the PSF and subtracted from the observed image to obtain the residual image. The residual image is used to calculate the residual flux profile, which is then added to the (unconvolved) best-fit Sérsic profile to obtain the corrected profile. r_{20}, r_{50} and r_{80} are then calculated by integrating this residual-corrected surface brightness profile.

Figure 1 displays the direct measurements of r_{80}/r_{50} and r_{20}/r_{50} ratios for 127 isolated galaxies in the GOODS-South field. We select these galaxies as being isolated if there is not another sources within ~ 10 r_{50}. Their size and magnitude distributions matches those of the overall sample. We use the H_{160} images to directly measure the different radii using the residual-corrected surface brightness profile as described above. We find that the direct measurements of r_{80}/r_{50} and r_{20}/r_{50} match the simple calculation based on the Sérsic profile well. This is consistent with studies that have shown that high-redshift galaxies are generally well fit by a single-component Sérsic profile (Szomoru et al. 2012). The scatter of the observed points around the Sérsic relation does not correlate with Sérsic index, redshift, or galaxy type, but it does increase for galaxies with $m_{\rm F160W} > 23$. Given the success in reproducing r_{80}/r_{50} and r_{20}/r_{50} based on the Sérsic index alone, we apply this simple calculation to the rest of our sample with the caveat that the values can be uncertain for individual galaxies.

3. The Distributions of r_{20} and r_{80}

3.1. The Size–Mass Plane

In Figure 2 we show the distribution of galaxies in the size–mass plane using three different measures of galaxy size: r_{20}, r_{50} and r_{80}. The size distributions are offset toward larger sizes when going from r_{20} to r_{50} and r_{80}, as follows from their definitions. However, we also find that the distributions of star-forming and quiescent galaxies are very different depending on which radius is used. Using r_{20} the two populations occupy separate regions of the size–mass plane with very little overlap. The quiescent galaxies are consistently smaller at a given stellar mass across the entire sample. The r_{80}-mass plane affords a different view. The star-forming and quiescent populations appear to follow the same distribution, with little difference between the two types of galaxies. The canonical size–mass distribution, using r_{50}, lies between these two extremes. The
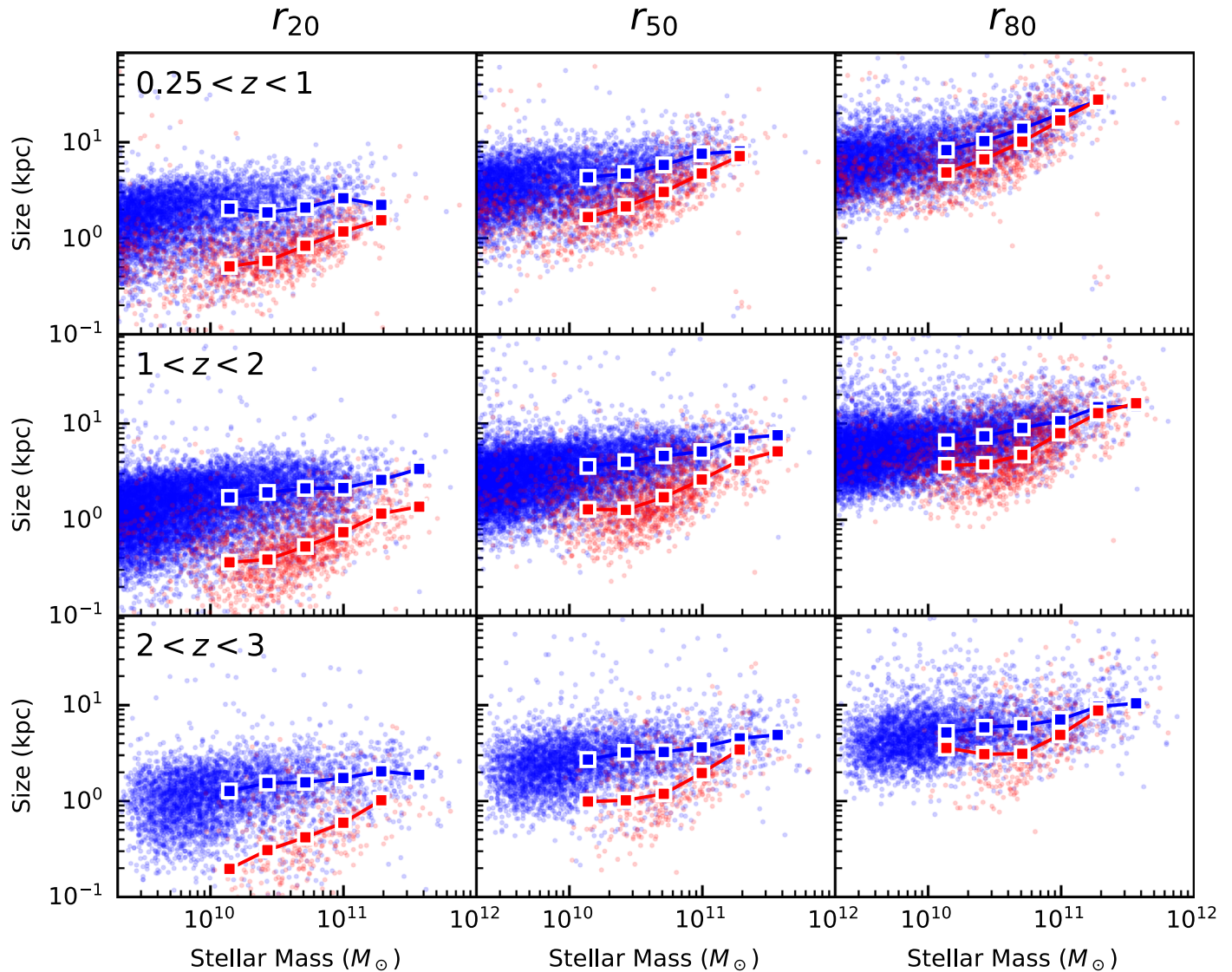
Figure 2. Size–mass distributions of galaxies using different measures of the size. Columns show the size–mass distribution using r_{20}, r_{50} and r_{80} as a measure of the size, while rows display different redshift bins. Blue and red points show star-forming and quiescent galaxies, and the squares show the median sizes in bins of stellar mass. At a given stellar mass the difference between star-forming and quiescent galaxies varies based on which measure of size is used. In r_{80} the two galaxy types largely overlap, whereas in r_{20} the star-forming and quiescent galaxies follow distinct distributions.

distribution of galaxies in this plane is often interpreted in the context of the distinct relations that star-forming and quiescent galaxies follow (see van der Wel et al. 2014; Mowla et al. 2018, and references therein), but as we show in Figure 2 this conclusion depends sensitively on the definition of size.

The distribution of r_{20} and r_{80} for star-forming and quiescent galaxies across a range of stellar masses and redshifts is shown in Figure 3. We observe that the two galaxy populations represent two distinct distributions of r_{20}, while they appear to follow the same distribution in r_{80}. The bimodality in the distribution of r_{20} is most clear for intermediate stellar mass ($10 < \log M_*/M_\odot < 11$) and high redshift ($z > 1$). Here the peaks of the distributions for star-forming and quiescent galaxies are clearly separated and a valley between the two distributions is apparent. By contrast, the distributions of r_{80} for the two populations are nearly identical. Across the entire range of stellar mass and redshift the peaks and widths of the r_{80} distribution appear at nearly the same location for star-forming and quiescent galaxies.

3.2. Bimodality in the Distribution of r_{20}

To highlight and quantify these trends, we focus on the distribution of radii in a single stellar mass and redshift bin in Figure 4. We investigate the overall distribution of sizes, without separating star-forming and quiescent galaxies. The distribution of r_{20} appears to be bimodal. To test this hypothesis, we employ Hartigan's dip test (Hartigan & Hartigan 1985), which tests the null hypothesis that the sample is drawn from a unimodal distribution.[4] When analyzing the logspace distribution of r_{20} in this mass and redshift bin we find $p = 0.043$, which means that the null hypothesis of a unimodal distribution can be rejected with $>95\%$ confidence. As an additional test, we fit one- and two-component Gaussian mixture models[5] to the logspace distributions of r_{20}, r_{50}, and r_{80} and compare the Bayesian information criterion (BIC) of each

---

[4] This test is computed using the R package `dip test` (https://cran.r-project.org/web/packages/diptest/).
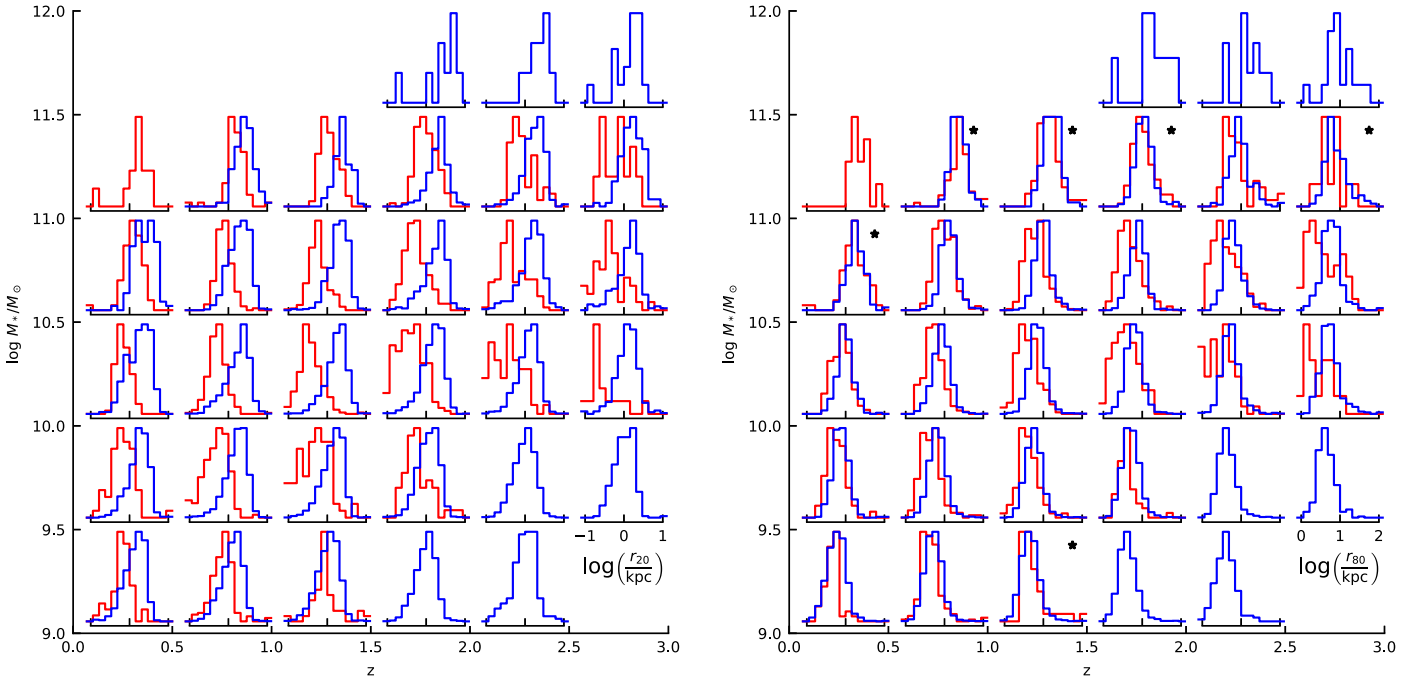[5] We use the `scikit-learn` python package (Pedregosa et al. 2011).

Figure 3. Distribution of galaxies in r_{20} and r_{80} for a range of stellar mass and redshift bins. Blue histograms display the distribution of star-forming galaxies and red histograms show quiescent galaxies. We only show histograms where the number of galaxies in that region of parameter space is greater then eight. Additionally, each histogram is normalized to the same height, so the relative heights of the distribution contain no information about the relative number of star-forming or quiescent galaxies in each bin. When considering r_{20}, star-forming and quiescent galaxies follow separate distribution, whereas in r_{80} the two types appear to follow the same log-normal distribution. Black stars in the r_{80} panel indicate bins where the Kolmogorov–Smirnov test concludes that the distribution of sizes for star-forming and quiescent galaxies could be drawn from the same parent distribution ($p > 0.05$).
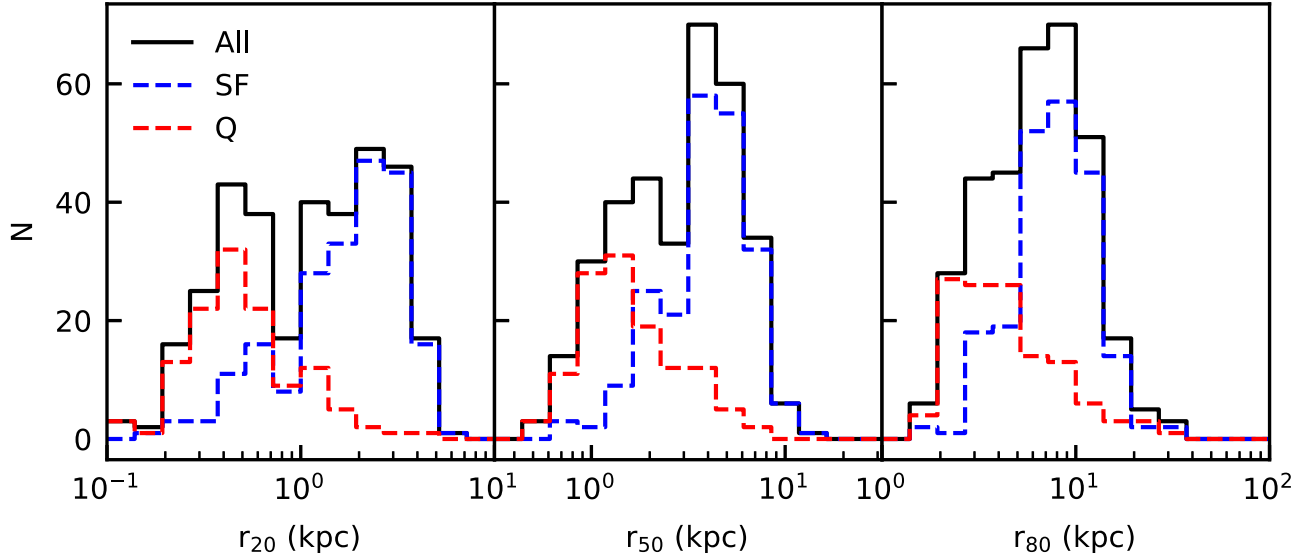

Figure 4. Distribution of r_{20}, r_{50} and r_{80} is shown for all galaxies in with $1.5 < z < 2$ and $10.6 < \log(M_*/M_\odot) < 10.8$. Also displayed are the distributions of star-forming and quiescent galaxies separately. A bimodality in the distribution of galaxies in r_{20} can be seen, even without dividing them into star-forming and quiescent. This is confirmed through Hartigan's dip test. Using Gaussian mixture models, we also show that the distribution of r_{80} is consistent with a single log-normal distribution (see the text).

model. Unsurprisingly, the distributions of r_{20} and r_{50} are better fit by the two-component model ($\Delta\mathrm{BIC} = \mathrm{BIC}_{1\,\mathrm{comp.}} - \mathrm{BIC}_{2\,\mathrm{comp.}} = 49.5$ and 41.5, respectively). Interestingly, for r_{80} we find that it is better fit by the single-component model ($\Delta\mathrm{BIC} = -5.3$).

In the top panel of Figure 5 we broaden this analysis and quantify the separation of the distributions of star-forming and

quiescent galaxies as a function of mass, redshift, and size definition. This is done through the Ashman's D parameter (Ashman et al. 1994), given by

$$D = \sqrt{2}\,\frac{|\mu(\log r_{\mathrm{SF}}) - \mu(\log r_{\mathrm{Q}})|}{\sqrt{\sigma(\log r_{\mathrm{SF}})^2 + \sigma(\log r_{\mathrm{Q}})^2}}. \tag{4}$$
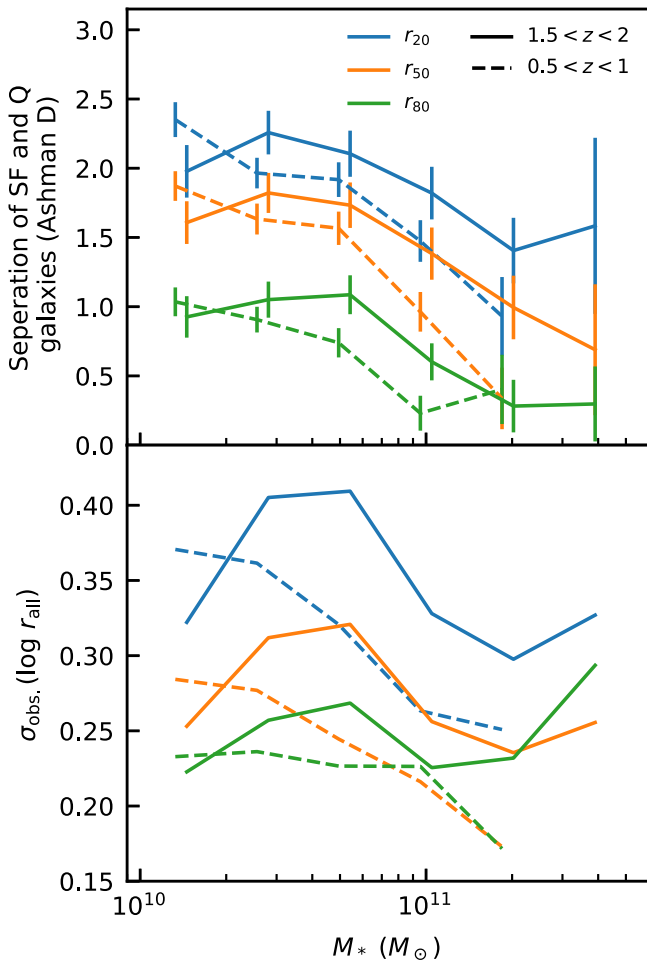
Figure 5. Top panel: evidence for bimodality in size distributions as quantified using the Ashman D parameter (Equation (4)). Bottom panel: the observed scatter, estimated using the bi-weight scale, in r_{20}, r_{50} and r_{80} as a function of stellar mass and redshift. The reduced bimodality for r_{80} leads to the smaller scatter.

Here, μ is the mean of each galaxy population and σ is the standard deviation, which we estimate using the bi-weight location and scale, respectively (Beers et al. 1990). In the ideal case of a combination of two identical Gaussian distributions, the combined distribution shows two distinct peaks if $D > 2$ (Everitt & Hand 1981). This threshold of $D > 2$ is also used more broadly to indicate when a distribution is bimodal, regardless of the functional form. The Ashman D values for r_{20}, r_{50}, and r_{80} are shown in Figure 5 as a function of stellar mass and redshift. At all masses and redshifts the difference between star-forming and quiescent galaxies increases when going from r_{20} to r_{50} and from r_{50} to r_{80}. For r_{20}, there is significant bimodality with $D > 2$ at all stellar masses in the range $1 \times 10^{10} < M_*/M_\odot < 5 \times 10^{10}$. The Ashman D value decreases at large stellar masses ($M_* > 10^{11} M_\odot$) for all size definitions, echoing the results of Mowla et al. (2018) for r_{50}. The Ashman D value for r_{80} is $\ll 2$ at all stellar masses and redshifts, consistent with the GMM analysis.

3.3. Implications for the Observed Scatter in the Size–Mass Relation

The fact that the separation of star-forming and quiescent galaxies changes for different size definitions has implications

for the scatter in the overall size–mass relation: it is significantly smaller for r_{80} than for r_{50} and (particularly) r_{20}. This is demonstrated in the bottom panel of Figure 5. The observed scatter, estimated using the bi-weight scale, is larger in r_{20} than in r_{50} by 0.08 dex, due to the fact that the distributions of star-forming and quiescent have a larger separation. The scatter in r_{80} (≈ 0.25 dex, independent of mass and redshift) is generally smaller than in r_{50}. We note that the observed scatter for the quiescent and star-forming galaxies as separate populations is also ≈ 0.25 dex at all masses and redshifts, regardless of the choice of size indicator. This implies that the reduction of the scatter in r_{80} with respect to r_{20} and r_{50} can be attributed to the fact that the size distributions of star-forming and quiescent galaxies overlap in r_{80}. We are showing the observed scatter in the sizes of galaxies, which is the combination of intrinsic scatter and observational uncertainty.[6] To decouple these two quantities would require a careful analysis of the observational procedures and how they affect uncertainties in size measurements. Instead, our goal is to compare the relative scatter of different measures of the size.

4. Discussion

In this Letter we have investigated the size–mass distribution of galaxies if r_{20} or r_{80}, the radii containing 20% of 80% of the light, is used instead of the traditional measure of r_{50}. When using r_{20} we find strong evidence of bimodality in the size distribution at fixed mass; to our knowledge, such a structural bimodality has not been observed before. The two peaks correspond to quiescent galaxies and star-forming galaxies. When using r_{80} the size distribution is narrow, and star-forming and quiescent galaxies follow very similar size–mass relations at all redshifts. The results presented here could have been anticipated from the well-known relations between quiescence, mass, size, and Sérsic index. Specifically, quiescent galaxies are observed to have a higher average Sérsic index, which means that r_{20}/r_{50} (r_{80}/r_{50}) is lower (higher) when compared to star-forming galaxies. In this sense, the results presented here can be seen as a re-casting of these relations into a convenient form.

Understanding the distribution of light within galaxies aids our understanding of how they assembled (Hill et al. 2017; Huang et al. 2018), and the r_{20} and r_{80} distributions may highlight specific and distinct physical processes. Based on our results it seems likely that r_{20} is related to processes that affect star formation and quenching. Specifically, there appears to be a connection between the structural bimodality discussed in this study and the well-known color/sSFR bimodalities (Strateva et al. 2001; Baldry et al. 2004). It had already been recognized that these bimodalities are connected to the central density of galaxies (Barro et al. 2014; van Dokkum et al. 2015; Tacchella et al. 2017; Whitaker et al. 2017). These studies suggest a central density or velocity dispersion threshold above which galaxies quench. At fixed stellar mass, galaxies with a lower r_{20} have a higher central density. Therefore, these quenching thresholds are qualitatively consistent with the clean separation of star-forming and quiescent galaxies in r_{20}.

Turning to r_{80}, this provides a reasonable proxy of the total baryonic extent. At the highest masses typical values of r_{80} reach ~ 20 kpc, and given the similarity of the distributions of

---

6 A similar analysis was done in van der Wel et al. (2012), who concluded that the observed scatter in r_{50} is dominated by intrinsic scatter in this regime.

star-forming and quiescent galaxies in the r_{80}-mass plane, it is tempting to link this size to halo properties. Several studies have suggested a constant scaling between stellar and halo radius (Kravtsov 2013; Somerville et al. 2018). This connection between r_{80} and the halos of galaxies is explored further in an accompanying Letter, Mowla et al. (2019). We note that the differences between r_{20} and r_{80} can also be interpreted in the context of dynamical timescales; for massive galaxies these are typically a factor of ~ 20 longer at r_{80} than at r_{20}. r_{20} is therefore sensitive to processes that can change rapidly, such as star formation rates or nuclear activity, whereas r_{80} should be more or less immune to those.

The work presented here is an initial investigation into the differences in the galaxy size–mass distribution when using r_{20}, r_{50} and r_{80}, with more detailed analyses to follow. We have not quantified the evolution of the slope or normalization of the size–mass relation of r_{20}. Describing these trends may give insight into galaxy quenching through cosmic time. For r_{80}, we refer the reader to Mowla et al. (2019), which details the evolution of the r_{80}-mass distribution and its connection to halo properties. Another improvement will be measuring the mass profile of galaxies. Recent studies have shown a relatively constant offset between mass-weighted and light-weighted r_{50} (Szomoru et al. 2013; Mosleh et al. 2017), but it is not clear whether that would also apply to r_{20} and r_{80}. Finally, it is important to continue developing non-parametric techniques for measuring the surface brightness profiles of high-redshift galaxies. Given current facilities it is technically challenging to map the inner structure of high-redshift galaxies, as the effective radius is comparable to the width of the PSF. Planned AO instruments on 30 m class telescopes, which are proposed to provide a factor of ~ 10 better resolution, will allow us to map the inner structure of high redshift galaxies directly.

ORCID iDs

Pieter van Dokkum ● https://orcid.org/0000-0002-8282-9888
Lamiya Mowla ● https://orcid.org/0000-0002-8530-9765
Arjen van der Wel ● https://orcid.org/0000-0002-5027-0135

References

Ashman, K. M., Bird, C. M., & Zepf, S. E. 1994, AJ, 108, 2348
Baldry, I. K., Glazebrook, K., Brinkmann, J., et al. 2004, ApJ, 600, 681
Barro, G., Trump, J. R., Koo, D. C., et al. 2014, ApJ, 795, 145
Beers, T. C., Flynn, K., Gebhardt, K., et al. 1990, AJ, 100, 32
Brammer, G. B., Van Dokkum, P. G., Franx, M., et al. 2012, ApJS, 200, 13
Capaccioli, M. 1989, in World of Galaxies, ed. L. M. des Galaxies (Berlin: Springer), 208
Carollo, C. M., Bschorr, T. J., Renzini, A., et al. 2013, ApJ, 773, 112
Dutton, A. A., van den Bosch, F. C., Faber, S. M., et al. 2011, MNRAS, 410, 1660
Everitt, B. S., & Hand, D. J. 1981, Finite Mixture Distributions (Dordrecht: Springer)
Ferguson, H. C., Dickinson, M., Giavalisco, M., et al. 2003, ApJL, 600, L107
Hartigan, J. A., & Hartigan, P. M. 1985, AnSta, 13, 70
Hill, A. R., Muzzin, A., Franx, M., et al. 2017, ApJ, 837, 147
Huang, S., Leauthaud, A., Hearin, A., et al. 2018, arXiv:1811.01139
Koekemoer, A. M., Aussel, H., Calzetti, D., et al. 2007, ApJS, 172, 196
Koekemoer, A. M., Faber, S. M., Ferguson, H. C., et al. 2011, ApJS, 197, 36
Kravtsov, A. V. 2013, ApJL, 764, L31
Lange, R., Driver, S. P., Robotham, A. S., et al. 2015, MNRAS, 447, 2603
Matharu, J., Muzzin, A., Brammer, G. B., et al. 2018, arXiv:1811.06548
Mo, H. J., Mao, S., & White, S. D. 1998, MNRAS, 295, 319
Momcheva, I. G., Brammer, G. B., van Dokkum, P. G., et al. 2016, ApJS, 225, 27
Mosleh, M., Tacchella, S., Renzini, A., et al. 2017, ApJ, 837, 1
Mowla, L., van der Wel, A., van Dokkum, P., et al. 2019, ApJL, 872, L13
Mowla, L., van Dokkum, P., Brammer, G., et al. 2018, arXiv:1808.04379
Muzzin, A., Marchesini, D., Stefanon, M., et al. 2013a, ApJS, 206, 8
Muzzin, A., Marchesini, D., Stefanon, M., et al. 2013b, ApJ, 777, 18
Ono, Y., Ouchi, M., Curtis-Lake, E., et al. 2013, ApJ, 777, 155
Pedregosa, F., Varoquaux, G., Gramfort, A., et al. 2011, The Journal of Machine Learning Research, 12, 2825
Peng, C. Y., Ho, L. C., Impey, C. D., & Rix, H. W. 2010, AJ, 139, 2097
Sérsic, J. L. 1968, Atlas de Galaxias Australes (Córdoba: Observatorio Astronomico, Universidad Nacional de Córdoba)
Shen, S., Mo, H. J., White, S. D. M., et al. 2003, MNRAS, 343, 978
Skelton, R. E., Whitaker, K. E., Momcheva, I. G., et al. 2014, ApJS, 214, 24
Somerville, R. S., Behroozi, P., Pandya, V., et al. 2018, MNRAS, 473, 2714
Strateva, I., Ivezic, Z., Knapp, G. R., Narayanan, V. K., & Strauss, M. A. 2001, AJ, 122, 1861
Szomoru, D., Franx, M., Van Dokkum, P. G., et al. 2010, ApJL, 714, L244
Szomoru, D., Franx, M., & Van Dokkum, P. G. 2012, ApJ, 749, 121
Szomoru, D., Franx, M., Van Dokkum, P. G., et al. 2013, ApJ, 763, 73
Tacchella, S., Carollo, C. M., Faber, S. M., et al. 2017, ApJL, 844, L1
Trujillo, I., Forster Schreiber, N. M., Rudnick, G., et al. 2006, ApJ, 650, 18
van der Wel, A., Bell, E. F., Häussler, B., et al. 2012, ApJS, 203, 24
van der Wel, A., Franx, M., van Dokkum, P. G., et al. 2014, ApJ, 788, 28
van Dokkum, P. G., Nelson, E. J., Franx, M., et al. 2015, ApJ, 813, 23
Whitaker, K. E., Bezanson, R., van Dokkum, P. G., et al. 2017, ApJ, 838, 19
Williams, R. J., Quadri, R. F., Franx, M., et al. 2010, ApJ, 713, 738